	Form Approved OMB NO. 0704-0188

Public Reporting burden for this collection of information is estimated to average 1 hour per response, including the time for reviewing instructions, searching existing data sources, gathering and maintaining the data needed, and completing and reviewing the collection of information. Send comment regarding this burden estimates or any other aspect of this collection of information, including suggestions for reducing this burden, to Washington Headquarters Services, Directorate for information Operations and Reports, 1215 Jefferson Davis Highway, Suite 1204, Arlington, VA 22202-4302, and to the Office of Management and Budget, Paperwork Reduction Project (0704-0188,) Washington, DC 20503.

1. AGENCY USE ONLY (Leave Blank)	2. REPORT DATE 12/20/2007	3. REPORT TYPE AND DATES COVERED Final Report Date: 07/21/03 to 07/20/07
4. TITLE AND SUBTITLE Dynamic Probing of High Strain-Rate Laser-Driven Shock Waves in Materials		5. FUNDING NUMBERS DAAD19-03-1-0211
6. AUTHOR(S) Todd Ditmire		
7. PERFORMING ORGANIZATION NAME(S) AND ADDRESS(ES) University of Texas at Austin, Office of Sponsored Projects North Office Bldg. A, 101 East 27th Street, Suite 4.300, Mail Code A9000 P.O. Box 7726, Austin, Texas 78713-7726		8. PERFORMING ORGANIZATION REPORT NUMBER 200202048-007
9. SPONSORING / MONITORING AGENCY NAME(S) AND ADDRESS(ES) U. S. Army Research Office P.O. Box 12211 Research Triangle Park, NC 27709-2211		10. SPONSORING / MONITORING AGENCY REPORT NUMBER 45037.1 - MS

11. SUPPLEMENTARY NOTES

     The views, opinions and/or findings contained in this report are those of the author(s) and should not be construed as an official Department of the Army position, policy or decision, unless so designated by other documentation.

12 a. DISTRIBUTION / AVAILABILITY STATEMENT Approved for public release; distribution unlimited.	12 b. DISTRIBUTION CODE

13. ABSTRACT (Maximum 200 words)

Work under this grant was focused on the probing of fast dynamics induced by laser driven shock waves. These studies are motivated by the fact that a complete understanding of shock waves in materials requires comprehensive microscopic understanding of the compression wave. Under our ARO grant we undertook a series of experiments to develop ways of studying atomic scale motions in materials as a material undergoes very high strain rate shock compression. To study these dynamics we used short pulse lasers in high time resolution pump-probe experiments. Our initial work concentrated on examining the shock induced melt transition in various materials including tin and silicon. First we utilized a series of linear optical diagnostics to characterize the shock strengths achievable with our short pulse laser. In addition to these linear optical probes, we then developed a non-linear optical probe involving the generation of third-harmonic photons at the surface of our target. Using this technique, we have observed the first real-time shock induced phase changes in silicon.

14. SUBJECT TERMS Shock waves in materials, high strain rate shock compression, shocks driven by intense laser pulses, third harmonic generation shock probing		15. NUMBER OF PAGES 31
		16. PRICE CODE

17. SECURITY CLASSIFICATION OR REPORT UNCLASSIFIED	18. SECURITY CLASSIFICATION ON THIS PAGE UNCLASSIFIED	19. SECURITY CLASSIFICATION OF ABSTRACT UNCLASSIFIED	20. LIMITATION OF ABSTRACT

NSN 7540-01-280-5500

Enclosure 1

Dynamic Probing of High Strain-Rate Laser-Driven Shock Waves in Materials

Final report for ARO Project DAAD19-03-1-0211

Principal Investigator:
Todd Ditmire
Department of Physics
University of Texas at Austin
Austin, TX
Phone: 512-471-3296
FAX: 512-471-8865
e-mail: tditmire@physics.utexas.edu

I. Introduction

Work under this grant was focused on the probing of fast dynamics induced by laser driven shock waves. These studies are motivated by the fact that a complete understanding of shock waves in materials requires comprehensive microscopic understanding of the compression wave. Under our ARO grant we undertook a series of experiments to develop ways of studying atomic scale motions in materials as a material undergoes very high strain rate shock compression. To study these dynamics we used short pulse lasers in high time resolution pump-probe experiments. Our initial work concentrated on examining the shock induced melt transition in various materials including tin and silicon.

In many cases of shock loading at high strain rates the material response is complicated by phase transitions such as lattice restructuring and melting [1-6]. These phase transitions have a dramatic effect on the failure strength of a shocked material. Yet, the dynamics of such phase transitions are not well known. For example, the time scale for shock induced melting of a solid may take place on a picosecond time scale or it may take many nanoseconds for the material to become amorphous under the heating induced by the passage of a shock. It was these questions which motivated the studies described here.

Our studies have been conducted with shocks driven by intense laser pulses. Using lasers focused to intensity up to 10^{14} W/cm^2 we can produce, over small scales, shocks with pressures up to 1 Mbar. These shocks are created by the rocket action that results from the ablation pressure of plasma heated at the target surface. This method of producing a strong shock has the unique advantage that the shock drive is directly synchronized to an ultrafast optical probe. To study phase change dynamics in laser driven shocks we used ultrafast laser probe pulses in high time resolution pump-probe experiments to develop a real time diagnostic on the phase of a shocked material. Our ultimate goal was to probe the entire phase history of a material as it shock compresses and releases.

We have probed these shocks with a variety of time resolved optical techniques developed under the three year period of the grant. These techniques take advantage of the fact that the shock

driving laser pulse can be split and then be used to probe the back side of a shocked target. This yields time synchronization which permits study of very fast dynamics in these shocks. Our initial emphasis is to study shock induced phase transitions with the hope of learning about the time history of these phase transitions. Melting is one phase transition which is of technological importance as it can have a dramatic effect on the strength and spalling of shocked materials when they are driven to high shock pressures. Consequently, observation of real time melting in shocked samples was a major thrust of our optical probing experiments.

In addition to these linear optical probes, we developed a non-linear optical probe involving the generation of third-harmonic photons at the surface of our target. The idea behind this is to implement a high time resolution diagnostic for shocked materials that can discern whether a material is crystalline or anisotropic (ie melted). Using third harmonic generation, this idea was first illustrated on a static target by Yakovlev [7]. Our diagnostic relies on the selection rules for third harmonic generation changing as a material changes from a crystalline structure to an isotropic or amorphous structure. When using a circularly polarized input probe, third harmonic generation is bulk-allowed for a crystalline material, but it is disallowed for an isotropic target. We have successfully implemented this idea for the first time on a shocked crystal allowing us quite unique time resolved information about the shock induced amophization of Si. We believe that this is a very significant advancement which will permit a new range of experiments which can probe the time dynamics of shock induced phase changes in materials.

II. Experimental Techniques Developed Under this Grant

Our main focus has been to take advantage of our ability to generate a synchronized optical probe with the shock drive. Because our laser is a high energy femtosecond laser this gave us some unique options in probing the state of the shocked material. Work under this grant principally utilized two probing techniques. The first was a well known approach to studying the state of heated materials, utilizing the variation in reflectivity as a material is heated. The second took advantage of the femtosecond durations of our probe pulse by generating third harmonic light from the heated/shocked target. This second approach is very powerful, as discussed below, because it provides unambiguous information about whether a material is crystalline or amorphous. Under this grant we have utilized this novel probe for the first time on a shock compressed sample.

II.A Linear Reflectivity

The simplest form of optical probe has to do with the reflectivity of the surface. The reflectivity depends on the complex refractive index and, therefore, directly depends on the conductivity of the sample. The refractive index can vary depending on whether the target is solid or liquid. The measured reflectivity, then, is related to the complex refactive index through the well known Fresnel equations [8]. For conducting targets, the refractive index can usually be described by a Drude model.

As described below, the majority of our experiments were conducted with Sn or Si targets (with a small fraction of results in Al and GaAs). Sn is metallic and therefore does not exhibit a large reflectivity change upon melting. The fall off of Sn reflectivity when it melts as a function of incident probe laser beam angle is illustrated in figure 1. The reflectivity is not expected to fall much below 90% at any incidence angle. We will note that this is at odds with observations made by Werdiger et al. on shocked Sn [5], who observed a large (>50%) drop in reflectivity in Sn targets shocked to a few hundred kbar. As described below, we observe a similar reflectivity drop which is as yet unexplained.
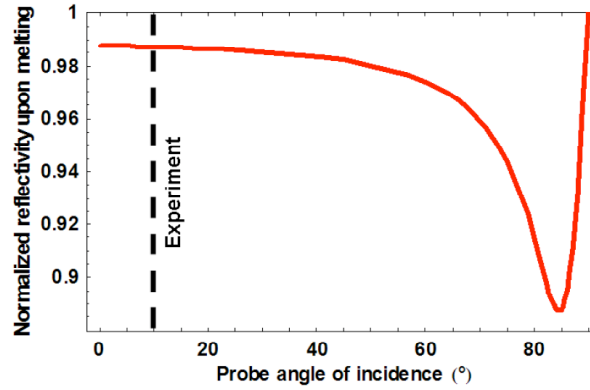
Figure 1: Reflectivity of 800 nm light off of melted tin normalized to unmelted tin as a function of incident probe beam angle.

Silicon, however, is expected to exhibit a much greater change in reflectivity under melting. As a crystal Si is a semiconductor however when melted Si becomes a reflective conductor. Figure 2 illustrates the expected reflectivity of Si as a function of incident angle for 800 nm light. We use this large change of reflectivity in melted Si to benchmark our principal probing technique, third harmonic generation.
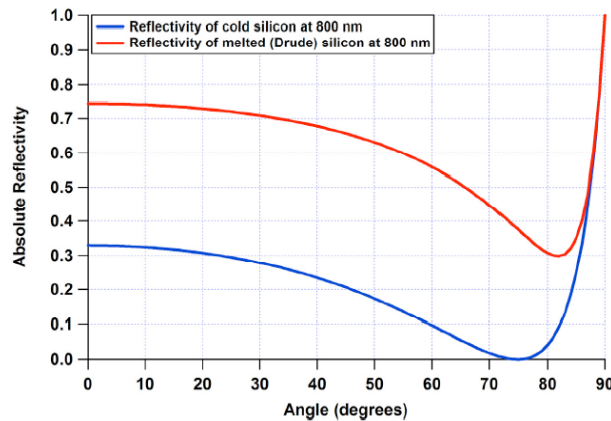

Figure 2: Reflectivity of 800 nm light off of melted and crystalline silicon as a function of incident probe beam angle.

II.B Shock Probing with Third Harmonic Generation

To gain insight beyond what simple reflectivity can give us, we have developed a novel technique that permits us to determine whether a shocked sample is crystalline or amorphous. The idea is illustrated in figure 3. By shocking a sample with a laser pulse, a second, synchronized laser can be directed at the back of the target and, if the intensity is sufficient, 3rd harmonic light can be generated. Standard nonlinear optical theories indicate that with circularly polarized light, this 3rd harmonic can only be produced if the sample remains crystalline and drops if it become amorphous. The advantage of this technique is that it is very sensitive, yielding information about whether the crystal melts even if the lattice develops only short range disorder. It is also less ambiguous than reflectivity because disordering is accompanied by a very large drop in 3rd harmonic signal.

As illustrated in figure 3, the general principal relies on probing the back surface of a shocked sample. To generate significant 3rd harmonic without ablating the material with the probe pulse, it is necessary to use a femtosecond probe. This probe will be converted to circular polarization and focused to an intensity of $\sim 10^{12}$ W/cm^2 in an area centered on the expected shock breakout region.
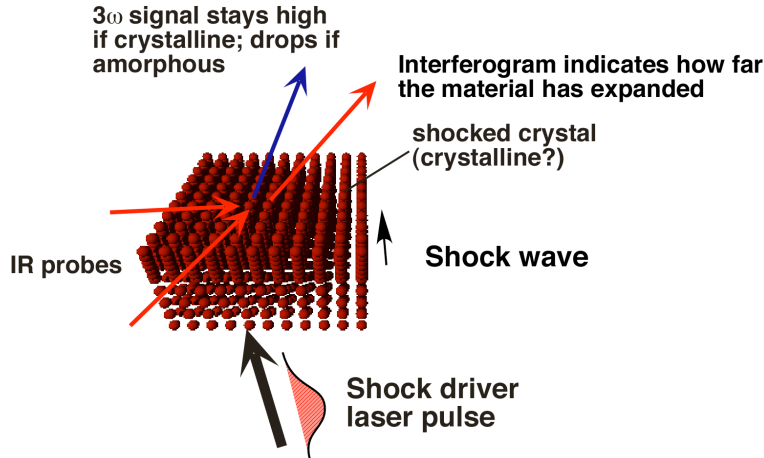

Figure 3:Cartoon principle of the 3rd harmonic shock probing technique developed under this grant.

How the third harmonic technique works can be illustrated through some simple nonlinear optical considerations. The amount of 3rd harmonic generated from illumination of the surface of some material is directly related to the square of the nonlinear polarization source term, $\vec{P}^{NLS}(3\omega_1)$. This term is related to the nonlinear susceptibility tensor, χ, and the cube of the incident electric field, E:

$$\vec{P}^{NLS}(3\omega_1) = \hat{p} P^{NLS}(\omega_3) = \chi(\omega_3 = 3\omega_1): \vec{E}^T \vec{E}^T \vec{E}^T e^{i(\vec{k}_z \cdot \vec{r} - 2\omega_1 t)} \tag{1}$$

In general, the point group symmetry of the non-linear material imposes certain restrictions on the form of the susceptibility. It is this effect that we take advantage of in being able to discern whether the sample is crystalline of amorphous. Equation (1) must be invariant under the

allowed symmetry operations of the medium. As an example, if we consider crystals with cubic point symmetry, this nonlinear source term simplifies to

$$\vec{P}_i^{NLS} = 3C_{1122}E_i(\vec{E}\cdot\vec{E}) + \left(C_{1111} - 3C_{1122}\right)E_i^3 \tag{2}$$

where C_{abcd} represents the tensor components of χ, and *abcd* are the directions of polarization. For an isotropic material, $C_{1111}=3C_{1122}$ so eq. (2) shows that the second term on the right hand side vanishes and the nonlinear source term will produce third harmonic such that a linearly polarized input electric field will yield a 3rd harmonic wave that is also polarized in the same direction..

Now consider the case in which the incident probe is circularly polarized. We assume, for illustrative purposes, that a right circularly polarized wave is normally incident upon a (100) oriented, cubic non-linear material. The incident electric field can be written as,

$$\vec{E} = E_o\hat{x} + iE_o\hat{y} \tag{3}$$

The non linear polarization source term in our cubic crystal is given by eq. (2). After plugging in our circularly polarized incident beam, we have can say that,

$$\vec{E}\cdot\vec{E} = E_o^2 - E_o^2 = 0 \tag{4}$$

so the nonlinear source becomes

$$\vec{P}^{NLS} = \left(C_{1111} - 3C_{1122}\right)E_o^3\left(\hat{x} - i\hat{y}\right) \tag{5}$$

and 3rd harmonic generation occurs with an intensity proportional to the square of eq. (2). However, as noted for an isotropic material, $C_{1111}=3C_{1122}$. In this case the right hand side of eq. (5) vanishes and no 3rd harmonic generation is allowed. An amorphous material (ie one that is beginning to melt) will fulfill this condition. In fact, as the crystal symmetry is broken the evolution of the eq. (5) toward the isotropic condition can in principle allow us to observe the time scale of this amorphization.

The physics behind the result of eq. (5) can be easily seen a different way. In 3rd harmonic generation we generate photons with frequency 3ω. Each 3 ω photon that is generated annihilates three 1ω photons. That is, the net change in angular momentum is,

$$\Delta m = \left|+3\hbar - (-\hbar)\right|$$
$$= \left|4\hbar\right| \tag{6}$$

Angular momentum of the system must be conserved, so it is taken up by the crystal lattice [9]. However, the (100) oriented cubic lattice can only absorb angular momentum in units of 4$\hbar$ because of the four-fold symmetry of the problem. If we were incident upon a (111) face, there is only a three fold axis of symmetry, and angular momentum can only be absorbed in units of 3$\hbar$. This explains why THG is disallowed from (111) orientations of cubic materials, but it is allowed for (100) orientations.

When the material is isotropic, angular momentum must be conserved. If the incident light is linear polarized, the net change of angular momentum is $\pm\,\hbar$ for each photon so a net zero

change in angular momentum is possible. However, for circularly polarized light, as eq. (6) indicates, the net change of angular momentum is not allowed in an isotropic medium.

II.C Experimental Design of Laser Driven Shocks

Using a laser to drive the shock has the distinct advantage of allowing one to generate a well synchronized optical probe for the shocked material. However laser driven shocks differ from other shock producing techniques such as HE or gas gun driven shocks in that the duration of the drive is much shorter (nanosecond time scale). This usually mandates the use of a very thin target slab. So a major aspect of our effort under this grant in the early period was to characterize the shocks driven by sub-ns laser pulses in target slabs only a few μm thick. In a schematic sense, figure 4 illustrates the time history of a compression wave in a sample driven by a finite duration laser pulse drive.
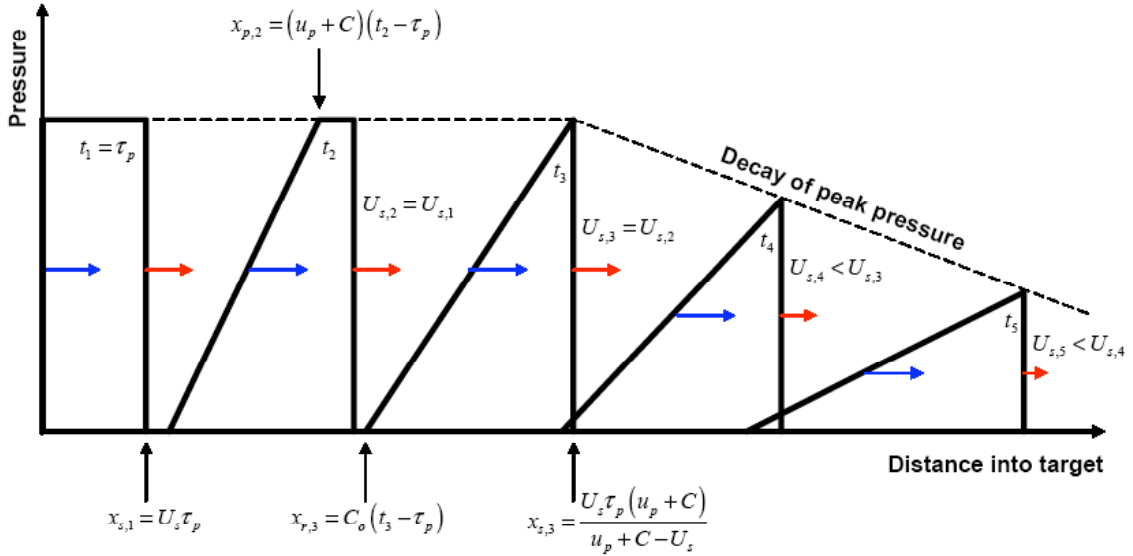
Figure 4: Schematic illustration of the interplay between the laser driven shock and the ensuing rarefaction wave from a finite drive pulse. Each pressure profile depicts an instant in the laser driven shock history.

In the time τ_p, the shock front will propagate to $x_s=U_s\tau_p$. At this point the laser drive is turned off (the pulse ends), causing a release wave to begin propagating behind the shock wave. The rarefaction (release) wave travels at the sound speed of the compressed material plus the particle velocity ($u_r=C_s+u_p$). This velocity is faster than U_s for normal materials ($\partial^2 P/\partial\rho^2 > 0$), which means that the faster traveling release wave will catch up to the shock front at position $x_{s,3}=U_s\tau_p(u_p+C_s)/(u_p+C_s-U_s)$. After this point, the release wave begins to decrease the peak pressure of the shock wave. As the pressure decreases, so will the shock velocity, causing the shock wave to slow down. In our experiments we needed to design carefully the target thickness and driven intensity to optimize the shock conditions at the back surface, while at the same time mitigating preheat of the material from the hot ablation plasma on the front surface. These constraints resulted in target thickness choices that were around 4-100 μm.

One of the principal tools that we employed in our experiment designs and interpretations was the Lagrangian hydrodynamics code HYADES [10]. An example numerical hydrodynamic simulation showing the propagation of a shockwave into a silicon slab is shown in figure 5. This HYADES simulation used a laser pulse with $I = 1.5\text{x}10^{13}$ W/cm^2, $\lambda = 800$ nm, $\tau_p = 460$ ps FWHM temporally peaked at 0.8 ns in the simulation. The target material was 300 μm of silicon, with a 300 nm overcoat of aluminum to absorb the laser. A curve fit to the peak pressures is displayed in the figure, and reveals an exponent close to that predicted by the self-similar solution for a blast wave [11]. It is this decay in peak pressure which limits our target thicknesses. However, it also allowed us to "tune" the shock pressure at the back surface by choosing various target thicknesses.
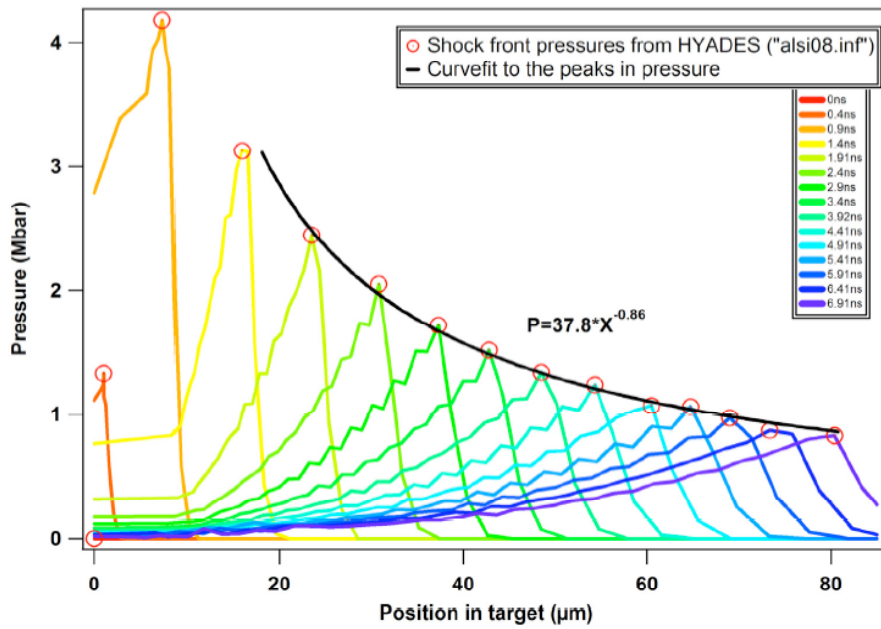
Figure 5: HYADES simulation of a shock wave/blast wave driven by a 460 ps pulse into a 300 μm silicon slab.

II.D Description of the THOR Laser

We have performed the experiments undertaken under this grant on the Texas High-intensity Optical Research Laser (the THOR laser) at UT. The optical schematic of this laser is illustrated in figure 6. This system is a Ti:sapphire, chirped pulse amplification laser which can deliver 0.7 J pulses with pulse duration under 40 fs at a 10 Hz repetition rate. It is composed of a 20 fs, 800 nm mode-locked oscillator stretched by a single grating all reflective stretcher to a pulse duration of 600 ps. These low energy pulses are amplified in a regenerative amplifier followed by a four pass amplifier and a five pass amplifier. The final amplifier yields pulses of 1.2 J energy with 600 ps duration. These 1.2 J pulses are compressed by a single grating compressor A vacuum tank houses the compressor and the pulse propagates in vacuum through a switch-yard to the target chamber in vacuum. For the experiments described in this document, we separated a large fraction of the uncompressed, 600 ps beam before it is sent to the compressor. By separating up

to 1 J, we derived a beam that could drive a strong shock. The remaining pulse energy was passed to the vacuum compressor where it was then employed as the synchronized probe.
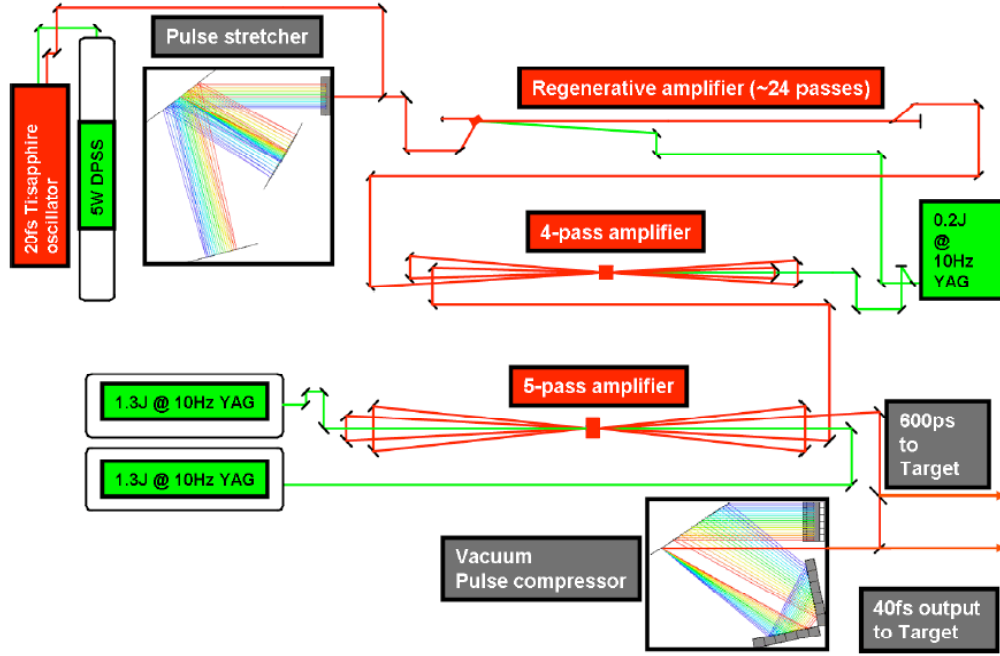

Figure 6: Optical schematic of the THOR Ti:sapphire laser used in the experiments performed under this grant.

For our experiments, we developed a vacuum chamber to house the targets, with time delay of the probe beam resting just outside this chamber. Figure 7 show an annotated photo of the shock chamber in the configuration used for the shock silicon experiments described in section V. The optical configuration will be described in that section.
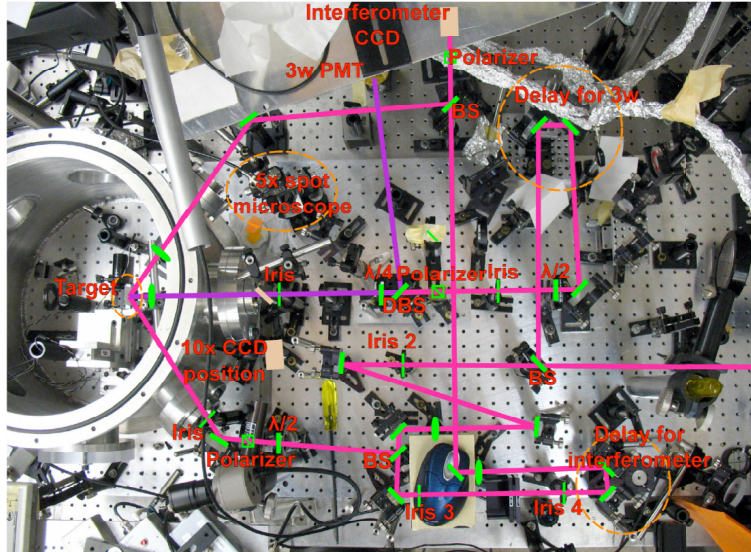
Figure 7: Photo of the target chamber constructed under this grant for the shock studies described in sections III, IV, and V.

III. Linear Reflectivity Probing of Shocks in Tin

The first phase of experiments performed under this grant involved laser driven shocks in tin. We chose tin because it is a solid which melts at a relatively low temperature. Because we have limited energy in our laser pulse to drive a shock (~ 1J) we are limited to lower drive intensities. This made tin an ideal candidate for our shock melting experiments.
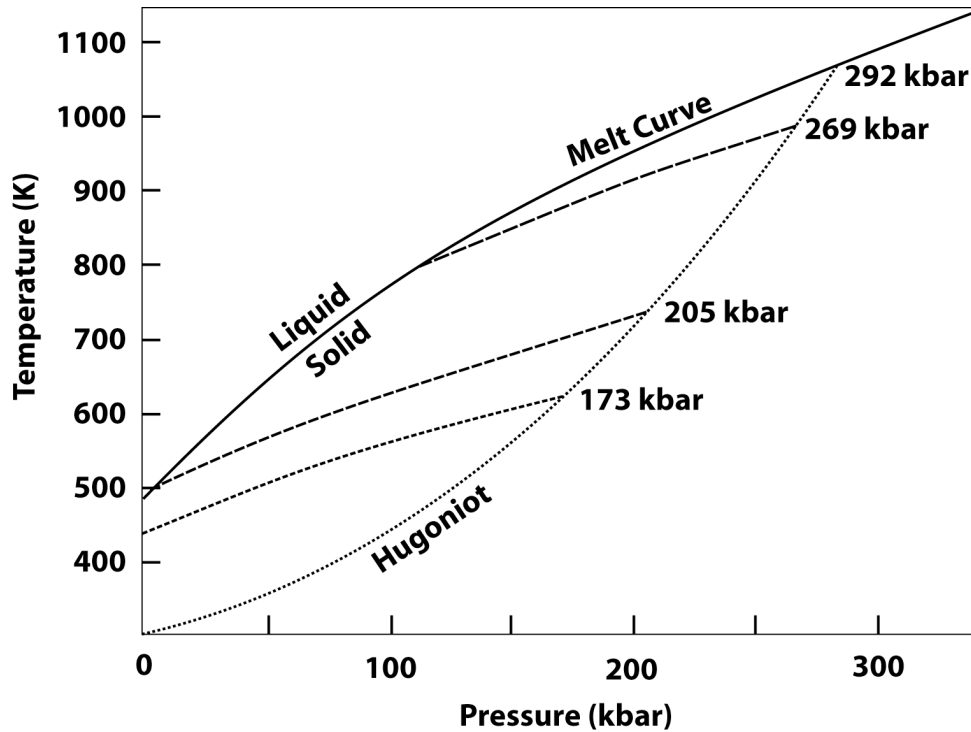

Figure 8: Phase diagram in tin showing the Hugoniot curve and various release isentropes. Adapted from ref [6].

Figure 8 shows the phase diagram of tin. Superimposed on this graph is the calculated shock Hugoniot [6]. The Hugoniot (dotted line) is shown to intersect the melt curve (solid line) at 292 kbar. So we expect that simple one-shock drive should lead to melted tin at shock intensity just above ~ 300 kbar, a pressure easily achievable with THOR. We also note that even if a shock is insufficient to melt the tin, we might expect it to melt once the shock releases from the back surface into free space. Various release isentropes (dashed lines) are shown labeled with their peak pressures. For pressures between 205 kbar and 292 kbar the material releases into the melt region of the phase diagram. For pressures below 205 kbar the material never melts, even upon release.

The shock experiments were performed inside of the specially designed vacuum chamber described in the previous section. Shooting the tin targets in vacuum allowed us to shock and probe without the worry of ionizing air near the focus of our beams. The shock driving laser was focused using an f/20 lens to a diameter of a few hundred microns FWHM, depending on the intensity for which we were aiming. The layout is illustrated in figure 9. The main laser pulse drove an ablation-driven shock wave which traveled through the target. The probe pulses used in these experiments typically had pulse durations of ~ 50 fs at the target surface (slightly

9

broadened from 35 fs by dispersion in transport optics) and energies in the 10 μJ to 1 mJ range, depending on how tightly the spot was focused. This led to probe intensities of order 10^9 to 10^{12} W/cm^2, where the lower intensities were typically used for reflectivity and interferometry, and the higher intensities were used to generate second and third harmonics.
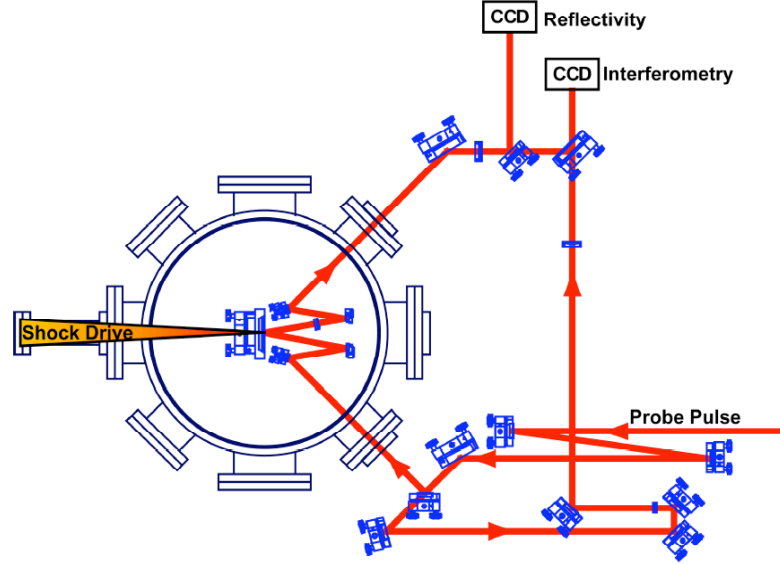

Figure 9: Optical layout of the shock experiments on tin.

For these experiments we employed two types of targets, free standing foils and tin layers adhered to a LiF window. These two target configurations are illustrated in figure 10. In general we chose targets with thickness near 4 μm. The target thickness was chosen so that the shock wave would not decay appreciably during propagation through the 4 μm of metal, while still allowing time for the shock to steepen. We performed considerable work in the early phases of this project to derive appropriate targets for these experiments. We found initially that commercially derived foils, usually produced by electroplating, did not have sufficient uniformity of thickness of quality.
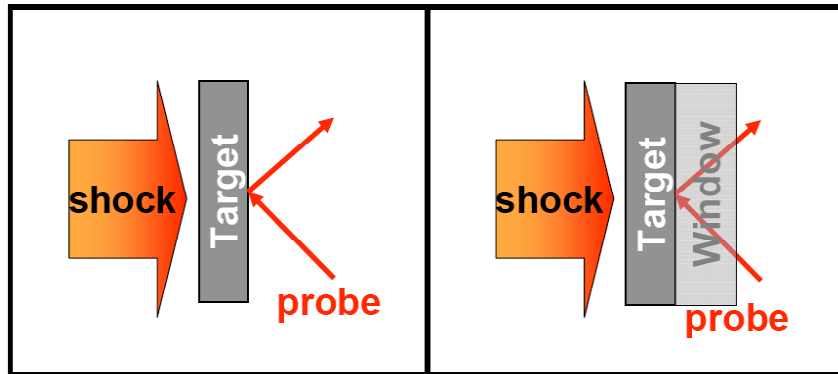

Figure 10: The two configurations employed in the thin tin target experiments.

Ultimately we produced in-house tin foils by vapor deposition of heated tin on glass slide. We derived optimum films when the slide was held at a temperature just below the melting point of the tin. [12] This allowed deposited tin atoms to migrate a short distance when they are deposited and fill in voids. These films were then floated off the slide in a soapy water solution. The other class of targets consisted of 4 μm of tin deposited onto the surface of a 50.8 mm diameter x 6 mm thick, (100) lithium fluoride window with a surface flatness of <= 0.3 μm. The window was used as a support structure for the thin foil, and also as a medium to confine the rear surface of the target to prevent material ejecta. These targets were mounted on a stage in the center of the target chamber. In order to shock and probe a fresh surface for each shot, an XYZ translation stage was used to raster the target between shots. We also note that we performed a small number of experiments on Al foils. These foils were procured commercially and were used to optimize the various diagnostics (as we did not expect any melting or other phase transitions in Al at the pressures we operate.)

The design of the targets was driven by a desire to match the shock transit time in the target to the drive pulse duration. This assures that a nearly constant pressure wave is driven throughout the target slab. We expected that a strong shock in tin, ie one above 300 kbar, will have a shock velocity of ~2000 m/s. Since our drive pulse duration was roughly 1 ns (the stretched pulse from THOR) we required thicknesses of $> 2 \mu m$. We were, however, also concerned with preheat of the target by the hot plasma as well as the possibility that targets only $2 \mu m$ thick would not be thick enough to allow the shock to develop into a steady state traveling wave. We therefore settled on targets that were between $4 \mu m$ and $6 \mu m$ thick. Numerical simulations were performed to derive a better idea of what sort of pressure waves we will achieve in our targets, particularly when the tin slab is coupled to a LiF window (which can lead to reflected shocks from the interface). Figure 11 illustrates a HYADES simulation of a $4 \mu m$ Sn slab coupled to a LiF window when the tin is driven by a 600 ps pulse at intensity of 8×10^{11} W/cm^2. We see from this simulation that the peak pressure (~ 250 kbar in this case) is indeed maintained until the shock reaches the back surface.

One of the main diagnostics used to determine shock parameters was a Mach-Zehnder style interferometer that probed off the back surface of the shocked material (see figure 9). To observe smooth and straight fringes with our probes, the surface flatness requirements were typically < 3 μm across the entire substrate. One arm of the interferometer traveled into the vacuum chamber, reflected off of the target interface, and was then imaged onto the face of a CCD camera located outside of the chamber. The reference arm of the interferometer was located completely outside of the chamber and was adjusted to have equal imaging optics and equal optical delay to the probe arm. A combining beamsplitter was placed before the CCD, and adjustments were made to straighten and optimize the fringes on the camera. Before each shot was taken, a reference image was saved so that the change in surface position due to the shock wave could be measured accurately. Data analysis was performed by Fourier analysis of the interferometric images, in a manner similar to Takeda, et al [13]. In this method, the image is first Fourier transformed, line by line. A super-Gaussian filter was then applied to the resulting spectrum to clean up the image. The new cleaned spectrum is inverse Fourier transformed and the phase shift is extracted from the result.
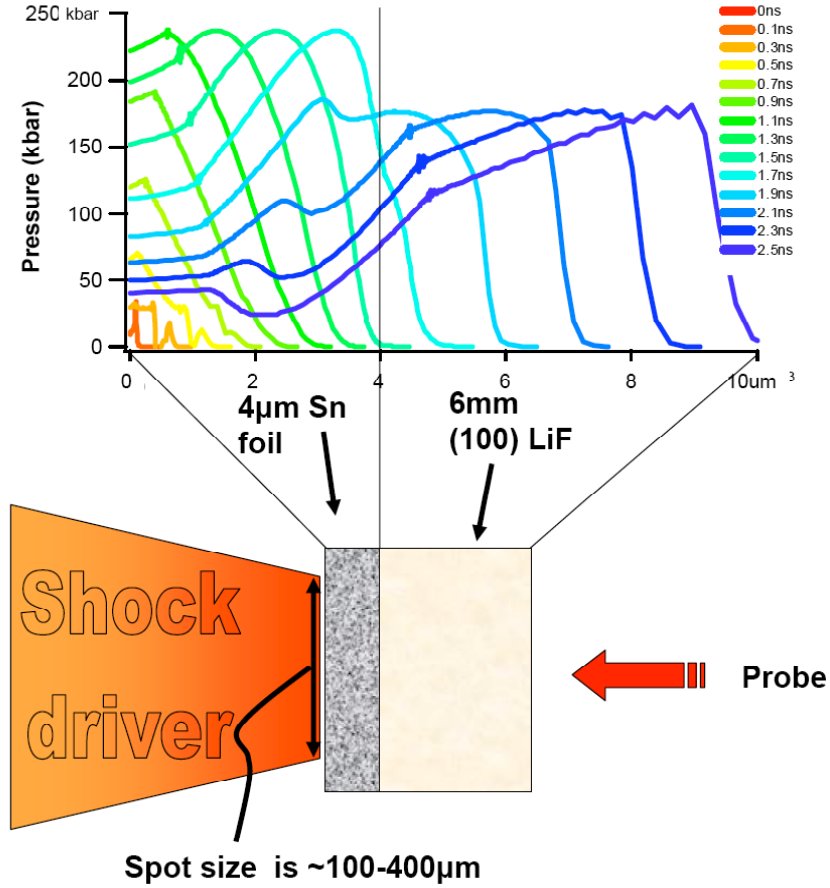
Figure 11: Results from a HYADES simulation showing various pressure profiles as a function of time in a Sn slab driven by an 800 nm pulse with duration 600 ps (Gaussian shape) focused to intensity of 8 x 10^{11}W/cm^2.

This diagnostic yielded two dimensional information about the shock breakout at the back surface for a given snap shot of time. An example of such a 2D interferogram is illustrated in figure 12. In this case the interferogram shows the shape of the shcok breakout from the tin into the LiF when driven by an intensity of 6 x 10^{12} W/cm^2 which corresponds to a shock pressure of 850 kbar (well above where we expect Sn to melt). The observed shock breakout nonuniformity resulted in large part from the nonuniformities in the drive laser intensity.

For these experiments in addition to interferometry, we employed a second diagnostic that measured two-dimensional linear reflectivity. Our reflectivity data was obtained with the same probe pulse as in the interferometer, however a beamsplitter diverted a portion of the probe arm to a separate 16 bit CCD camera before the beam was combined with the reference arm. This allowed us to obtain data with high resolution, and also without the added convolution that fringes cause in the interferometer. The reflectivity data was normalized to reference shots taken before the shock wave was driven into the target, so that we could more easily compare multiple shots with each other.
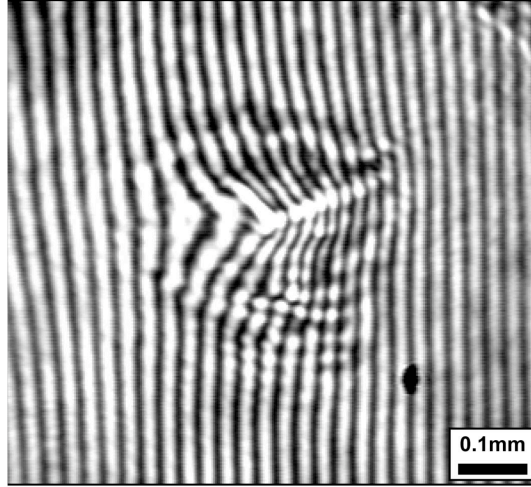
Figure 12: Example 2D interferogram of a shock breaking out from 4 µm Sn into at LiF window. The drive intensity was 6 x 10^{12} W/cm^2.

Our first priority was to characterize the shocks in these small metallic targets. We needed to determine the quality of the shock and breakout shape. Another question that stood out was whether a shock can reach quasi-equilibrium conditions in such thin samples. The Hugoniot relations are predicated on a steady-state flow of material across the shock interface. Whether a shock formed on the sub-ns time scale would meet these conditions was the topic of our early investigations.

Figure 13 illustrates the deconvolved expansion of the shock break-out from two focal spot sizes. The top compares the expansion 1 ns after initial irradiation with the focal spot optical intensity on target where the spot is roughly 150 µm in diameter. It can be seen that the shock break out follows the intensity profile very closely. The bottom two images also compare the laser intensity profile with the shock break out, with the laser defocused to ~ 500 µm. Again, the shock break out region is larger and follows more or less the intensity profile of the laser spot. These data show that we can indeed produce good clean shock waves in the thin tin with profiles that track the shape of the irradiating laser.

With data such as that in figure 13, we were then able to track the time history of the shock expansion. Figure 14 shows the expansion as a function of probe laser delay of shocks driven in free standing Sn and Al targets. The peak intensity of the drive laser was varied to change the shock pressure. The velocities we observe are consistent with shock pressures derived from the Hugoniot of between 75 and 220 kbar. This matches our Hyades simulations very well.

We conducted a similar campaign of measurements in the Sn/LiF combinations. We used five different laser intensities to drive shock waves into Sn/LiF targets. Again, we measured the displacement of the interface as a function of probe delay for each of these five cases. The maximum displacement that we could probe was limited by the fringe size relative to the shock spot, and also by the contrast between adjacent fringes on the CCD. For example,
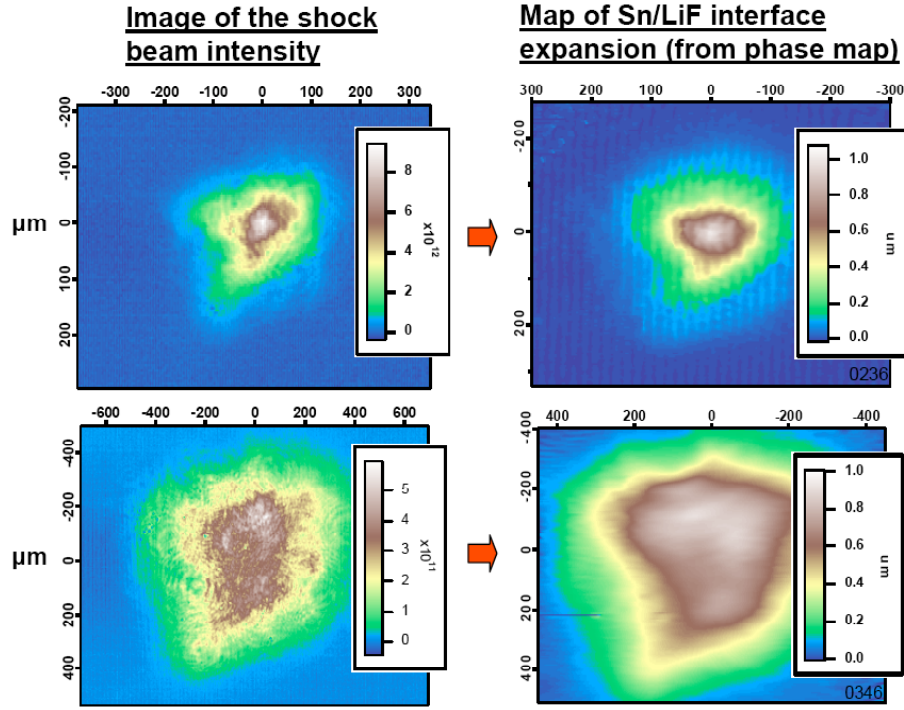
Image of the shock beam intensity

Map of Sn/LiF interface expansion (from phase map)

Figure 13: Left hand images are a false color rendition of the laser focal spot with peak intensity of 8 x 10^{12} W/cm² on the top and 5 x 10^{11} W/cm² on the bottom. Compared at the right are the deconvolved interferogram images from these shots showing how far the surface has expanded from the break out of the shock 1 ns after initial irradiation. In both cases the shock spatial distribution follows the intensity of the laser irradiation.
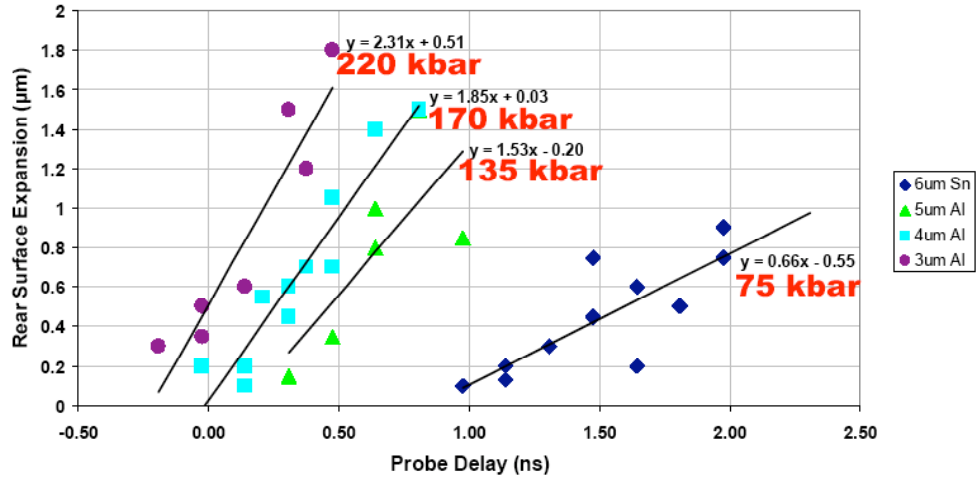
Figure 14:Pump probe data showing the expansion of shocks breaking out of free standing Sn and Al films as a function of time for various drive intensities. The pressures are derived from published Hugoniot curves for these two materials.

14

interferometric data for the 1×10^{13} W/cm^2 scan did not extend past 0.6 μm because of a lack of magnification in the probe imaging. For the other scans, where the fringes were distinguishable, we were able to observe up to a 2.1 μm expansion.

A line was fit to the linear portion of the expansion data, illustrated in figure 15, using a least-squares algorithm, to determine the particle velocity at shock breakout. The shock impedance mismatch between the tin and the lithium fluoride was accounted for so that the interface velocity could be converted into a particle velocity of the bulk tin. This particle velocity was then combined with Hugoniot data for tin to estimate the pressure observed at the interface within the target. The shock pressures derived from comparison with published Hugoniot data are shown in the first two columns of table 1.
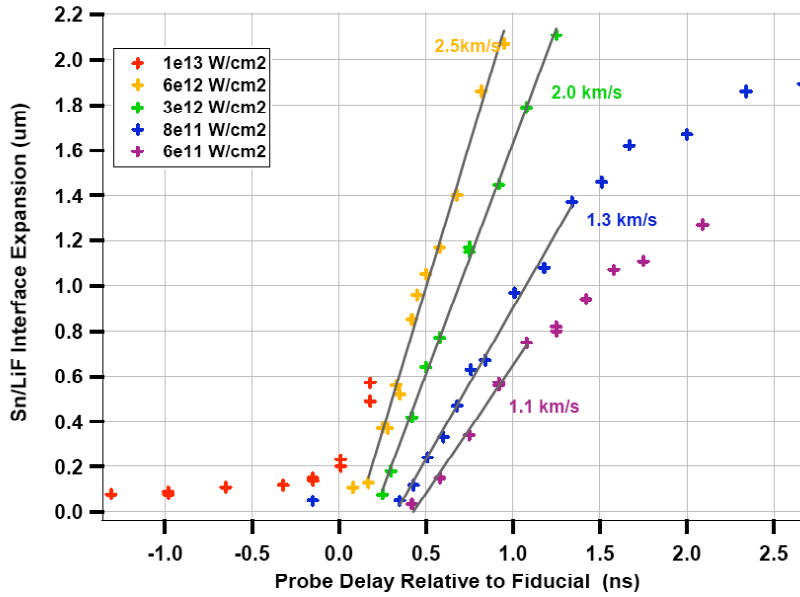

Figure 15: Pump probe data of shocks expanding from tin into the LiF window, probed through the window. Expansion data at five different peak drive intensities are shown and a line is fit to the early time history of each curve to derive a particle velocity which can be compared to the Hugoniot.

Incident Laser Intensity (W/cm^2)	Pressure From Measured U_p Using the Hugoniot (±30kbar)	Laser Intensity Used in HYADES Simulation (W/cm^2)	Pressure From HYADES Simulation (kbar)
6×10^{11}	271	8×10^{11}	237
8×10^{11}	341	1.5×10^{12}	380
3×10^{12}	617	3×10^{12}	645
6×10^{12}	853	5×10^{12}	950
1×10^{13}	N/A	N/A	N/A

Table 1: Shock pressures in Sn derived from comparison with published Hugoniot data and found by fitting numerical simulations of the shocks to the measured data points.

We wished to derive the shock pressures from a more sophisticated analysis of the data. To do this, we used HYADES to simulate the shock release into the LiF and calculate the surface of the tin/LiF interface as a function of time. We did this for various intensities and compared the curves to our measured data. We then chose the HYADES simulation that best fit our observed data comparing the simulated intensity to the actual measured intensity. Then we ascertained the shock pressure from the best fit simulation for each data set. The comparison of the best fit HYADES simulations replotted on the expansion data of figure 15 are shown in figure 16. As can be seen HYADES does a remarkable job of reproducing the shock expansion data. The best fit HYADES simulated intensities from this exercise are compared to the measured intensity in table 1. There is very good agreement between the measured intensity and the best fit simulated intensity, lending confidence in HYADES as a predictive tool for our experiments. The shock pressure derived from the best fit HYADES simulations are also shown in table 1. The pressures derived from this exercise match the pressures we simply derived from the expansion velocity and the Hugoniot to within about 15% in all cases.
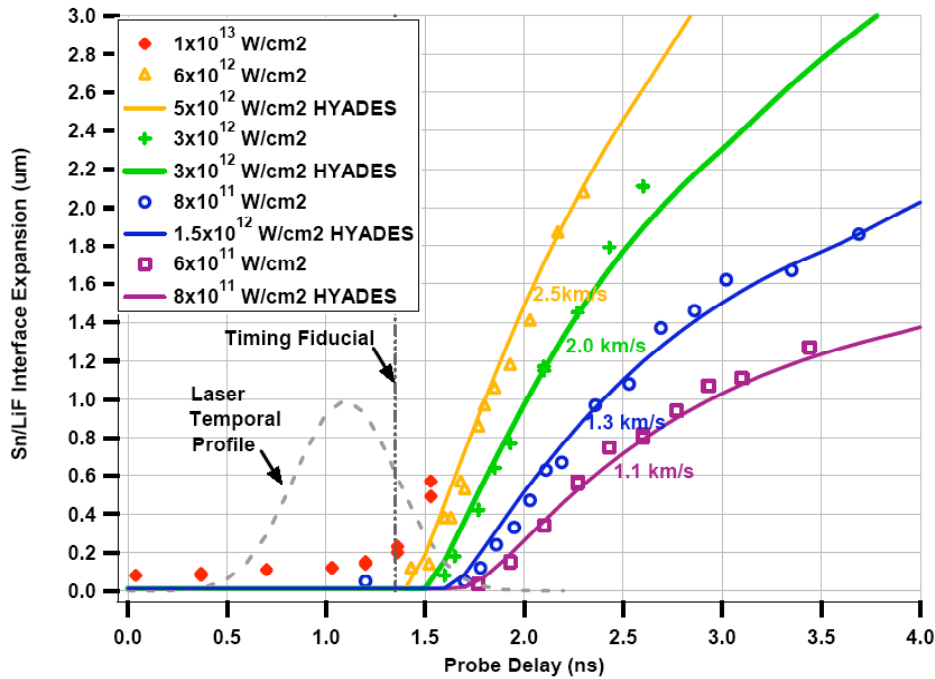

Figure 16: Pump probe data of shocks expanding from tin into the LiF window, probed through the window. Expansion data at five different peak drive intensities are shown and the best fit HYADES simulation of the shock break-out expansion is over laid on each data curve.

The conclusion that we draw here is that we can produce shocks in tin with pressure up to nearly 1 Mbar and that we can diagnose them well via our 2D interferometry technique. Furthermore, we can have good confidence in HYADES ability to simulate these shocks as the code reproduces the trends of the data exceptionally well.

Our next data campaign centered on making an independent measurement of the Hugoniot in tin. To do this, we required simultaneous knowledge of the particle velocity in the shock and the

shock velocity. The first quantity is derived from data similar to that of figure 15 in which we measure particle velocity by taking many pump probe shots and plotting the expansion as a function of time. From free standing foils $U_{particle} = U_{expansion}/2$. To derive the shock velocity we performed a similar set of experiments in foils of varying thickness. By measuring the shock break out time, namely the time at which the back surface begins to expand, for different target thickness, we could derive the shock speed. We performed shock breakout measurements for targets with thickness between 4 and 6 μm.

Figure 17 shows the results of this measurement in free standing tin foils and figure 18 shows the measurement performed on Sn folis overlaid in LiF. In the first case our data are compared to data previously published from Russian gas gun measurements [14] and in the second case our data are compared to the Hugoniot of the Los Alamos SESAME table [15] (the table used in our HYADES simulations.) In both sets of measurements there is very good agreement with the previously published gas gun data (up to the 850 kbar pressures of our measurements) and the SESAME table. This is a very important result as it confirms that shock measurements in these thin laser-driven targets yield results similar to measurements derived in other, more traditional, ways.
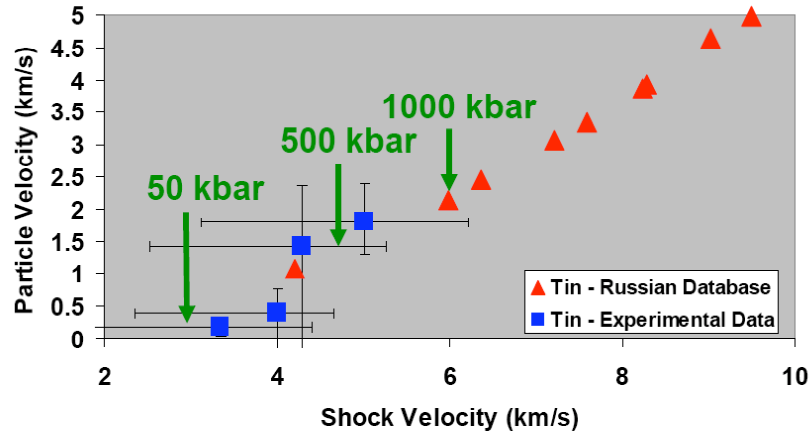

Figure 17: Measured Hugoniot of tin up to 850 kbar using our multi-pulse pump probe technique with free standing Sn foils compared to the data of ref [14].

We also measured the reflectivity of the tin both from free standing foils and the Sn/LiF targets. These experiments led to some rather unexpected results which will require future work to understand. As described above, we illuminated the entire shock break-out region just before the shot to get a calibrated map of the target surface reflectivity and then we again measured the reflected profile as the shock breaks out. Compare these "before" and "after" images allowed us to measure the 2D reflectivity as a function of probe delay. Characteristc data taken in this manner is illustrated in figure 19. These data were taken well after the shock breakout (46 ns) and show a significant drop in reflectivity in the center of the probe spot, where the shock has broken out from the Sn slab.
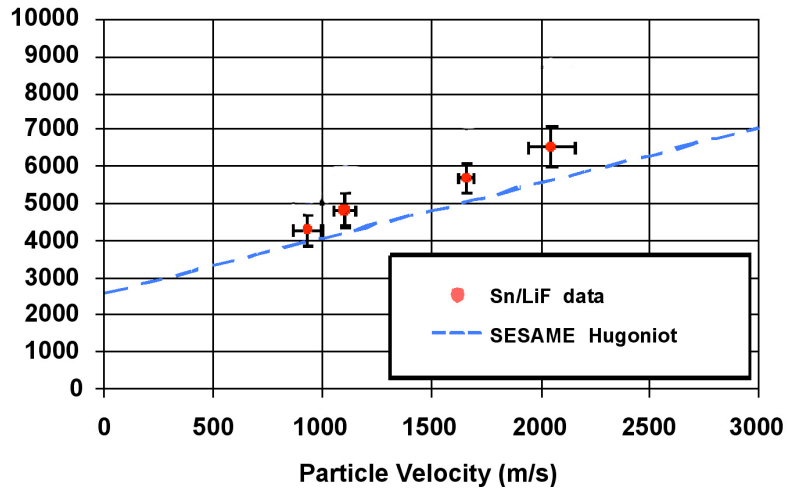
Figure 18: Measured Hugoniot of tin showing shock velocity vs particle velocity using our multi-pulse pump probe technique with Sn slabs on LiF. These data are compared to the LANL SESAME table predictions [15].
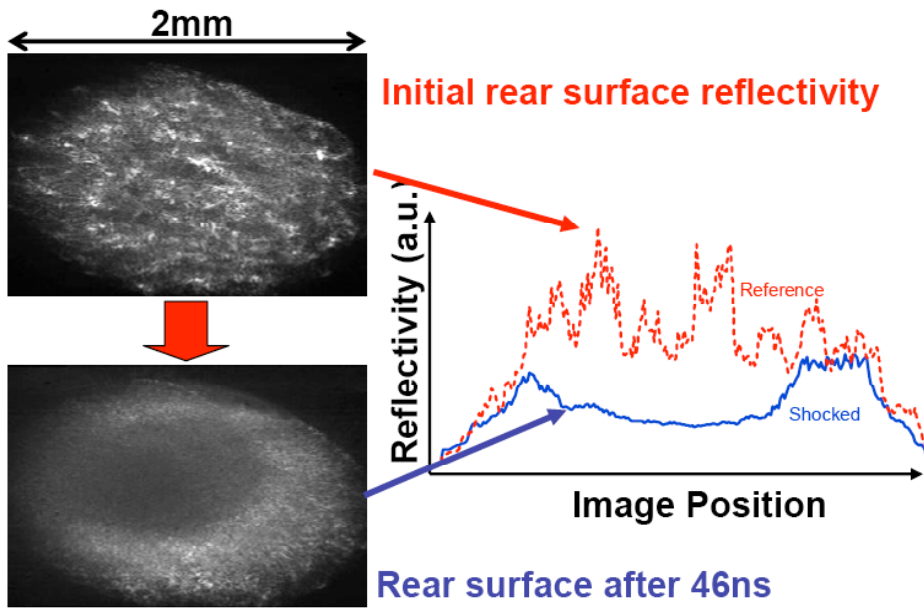

Figure 19: Probe images from the back side of a tin target before and after the shock has emerged from the slab. There is a significant drop in observed reflected light in the center of the target.

The peak reflectivity can then be plotted as a function of time by varying probe delay. Such a measurement is shown in figure 20 compared to the measured target surface expansion. The blue points show the expansion and reflectivity in the center of the spot for free standing foils and the red points show the same for Sn foils on a glass slide. We find the rather surprising result that the reflectivity drops on a 1 ns time scale to only 35% of its initial value. This is surprising as we expect only a small drop if the reflectivity were to be altered only by a melting transition. It is interesting that this large drop is similar to that seen in laser shocked tin by Werdiger et al. [5].
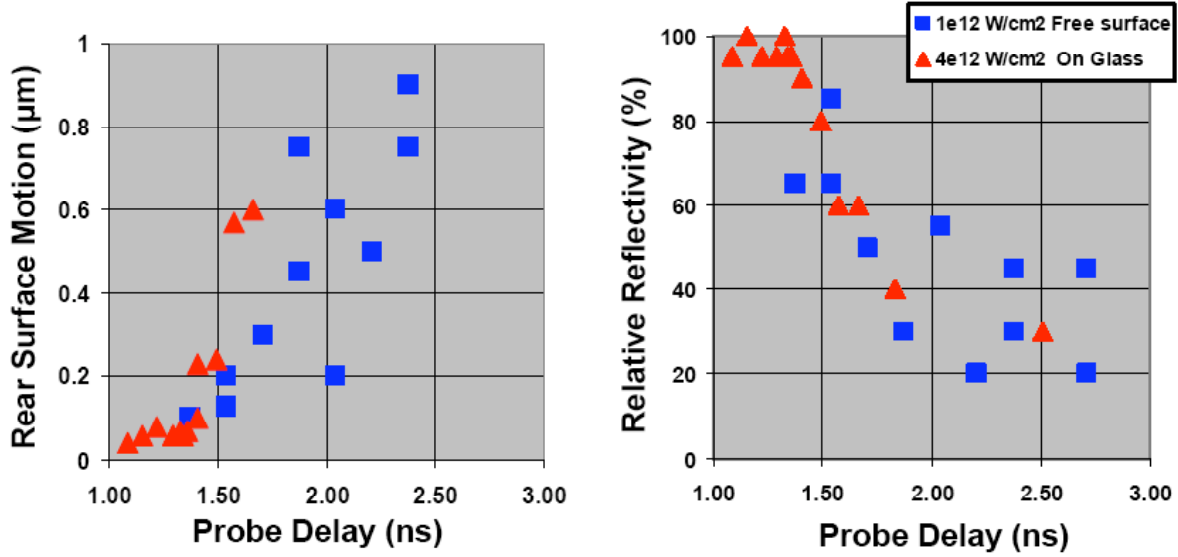

Figure 20: Left plot shows the expansion of the tin back surface as a function of time for both free standing and on-window tin. The right plot shows the reflectivity for these two cases over the same time window.

Our initial concerns were that this drop could be attributed to the formation of ejecta particles on the back surface seeded by the small grain sizes of our poly-crystalline targets. This is illustrated schematically in figure 21. However, we repeated the measurement with the tin layered on a window, a situation which presumably retards the formation of particles on the back surface. These data are also shown in figure 20 and exhibit a virtually identical drop in reflectivity over about 500 ps. This result is unexpected and as yet unexplained. One possibility is that micro-instabilities do develop at the interface and scatter the probe radiation. This may be a consequence of the loss of material strength that occurs when the material melts. However, much more work will have to be done to determine what is happening at this shock front.

Nonetheless, this phase of work was productive in that it demonstrated that laser produced shocks in thin samples over small scales in possible and that we can control and effectively model these shock at pressures up to 1 Mbar.
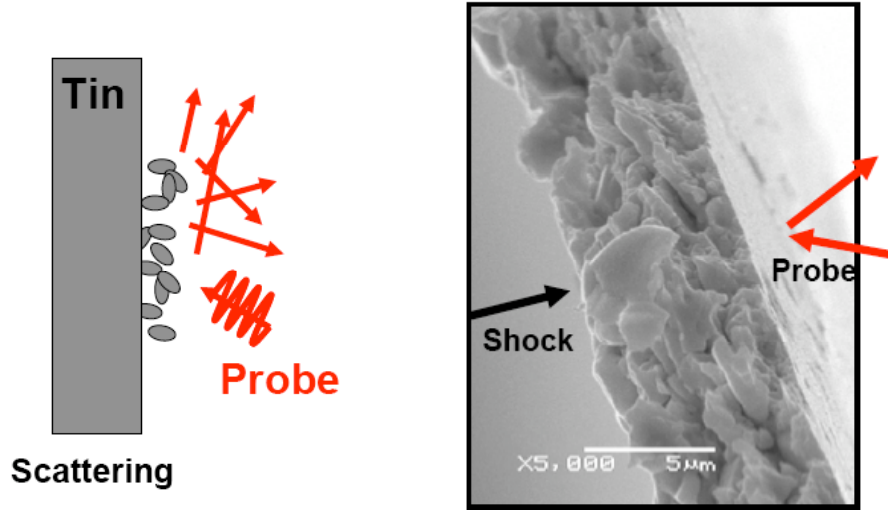
Figure 21: Schematic illustration of one possible explanation for the large drop in reflectivity observed from free standing shock tin foils.

IV. Third Harmonic Probing of Laser Heated GaAs and Si

The next phase of work under this grant revolved around developing the third harmonic generation diagnostic technique. To develop the technique, we decided to implement it on samples that were melted by direct laser heating before implementing it on a laser shock. This had the advantage of avoiding the initial complications of the shock driver and it allow us to compare the results of our technique with those of other laser induced melting studies performed with other techniques.

As noted above, harmonic generation (HG) is a powerful technique for probing long-range crystalline order. Previously in pump-probe experiments, second harmonic generation (SHG) has been used to identify a transformation of crystalline GaAs to a centrosymmetric electronic state within 100 fs [16]. It has also been used to discover a loss of cubic order in crystalline silicon within 150 fs of intense laser excitation [17]. Tom, *et. al*. discovered that 75 fs laser excitation of silicon above a threshold fluence causes bulk atomic disorder with a 1/e time constant of ~ 100 fs . In contrast, they found that the electronic properties, as determined by linear reflectivity, did not reach those of molten silicon for several hundred femtoseconds. This indicated that silicon was melting non-thermally before the lattice had time to equilibrate thermally. The dense electron-hole plasma created by the ultra-fast optical excitation weakens the atomic bonds, causing disorder in the lattice. This non-thermal process skips the "normal" thermal transfer of energy from the electronic system to the lattice by phonon emission., as the atoms remain cold for several hundred femtoseconds or more [18].

For many materials and crystallographic orientations, SHG is not dipole allowed in the bulk material, so detection of the small surface generated signals can be very difficult, especially for single shot type experiments. This is one of the principal reasons we chose to explore third harmonic generation (THG) as a shock probe under this grant. As discussed in section II, THG

is bulk-allowed in most crystalline materials, but disappears in isotropic media with circularly polarized excitation. For this phase of experiments, we chose to explore laser induced melting of Si and GaAs crystals, both of which can be procured easily with very high optical quality.

A cartoon of the set up for these experiments is illustrated in figure 22. In these experiments, we monitored the linear reflectivity and THG from the surface of bulk Si or GaAs wafer while pumping the same side of the target with a laser fluence near the melting threshold. For GaAs we also monitored second harmonic generation. The THG diagnostic operates by measuring the third harmonic light generated in reflection at the rear surface of the target from a circularly polarized, normally incident, 800 nm probe. The THG was measured using a Hamamatsu UV sensitive side-on PMT biased to ~ -1000 V. The PMT was connected to our Tektronix oscilloscope to record the data. The pump beam was a 40 fs pulse with a fluence of a few hundred mJ/cm^2 that was incident onto the target at an angle of ~ 17° off of normal. This pump pulse non-thermally melted the semiconductor in less than a few hundred femtoseconds. We utilized a wide angle, 58.5°, reflectivity probe to detect the large increase in reflectivity that occurs near Brewster's angle. At normal incidence, the circularly polarized harmonic generating probe was focused onto the target at a fluence less than 100 mJ/cm^2 to keep from damaging the target. The residual 800 nm not involved in THG was directed onto a photodiode so that reflectivity at normal incidence could be recorded.
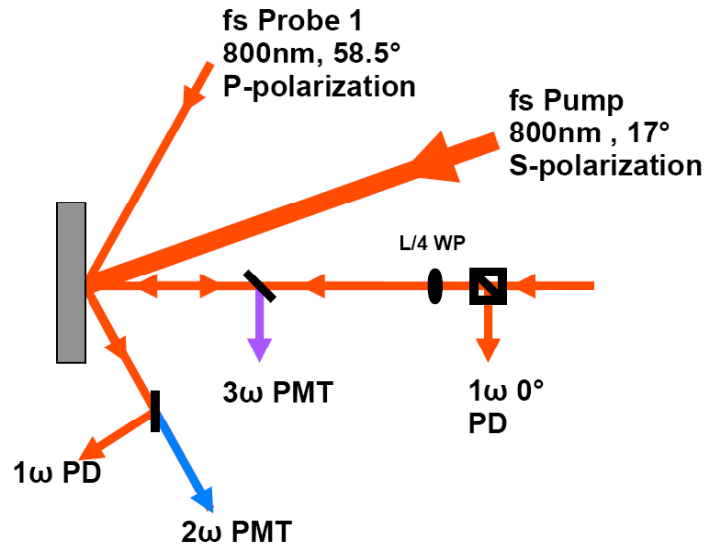

Figure 22: Schematic of the laser melted harmonic generation experiments.

The measured reflectivity and THG signal for both circularly and linearly polarized pump beams on GaAs are shown in figure 23. Similar data for laser induced melting in Si are shown in figure 24. Both sets of data look similar. As both crystals melt they transition from a semiconductor to a molten metallic material. Therefore there is alarge increase in reflectivity at 800 nm (the wavelength of the probe beam of THOR).

As the probe pulse delay was scanned relative to the pump pulse, a fast (less than 500 fs) transition was detected by both the reflectivity diagnostic, as well as the third harmonic

diagnostic in both Si and GaAs crystals. This agrees with previously published results [17,18]. This drop in harmonic generation (GaAs and Si) indicates a loss of electronic structuring of the target, which is confirmed by the large increase in the reflectivity probes (GaAs and Si). The spike in THG observed near *t=0* is a coherent artifact, arising from the temporal overlap of the probe and pump pulses.
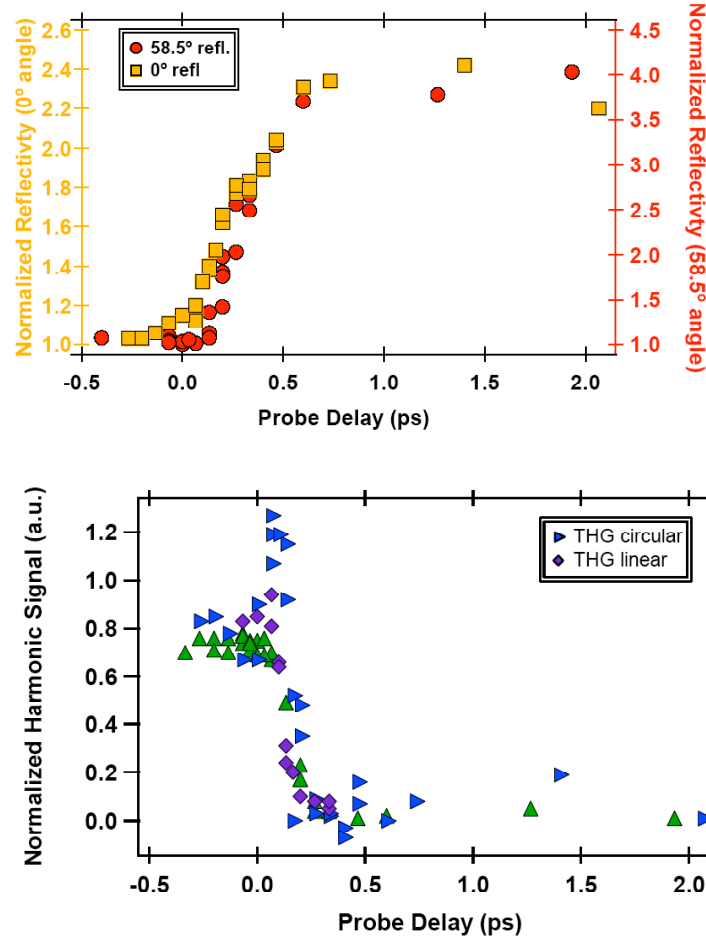

Figure 23: Reflectivity (top) and third harmonic signal (bottom) from two incident polarization configurations on the (100) surface of laser melted GaAs. These data are plotted as a function of probe delay. The pump laser fluence was 310 mJ/cm^2.
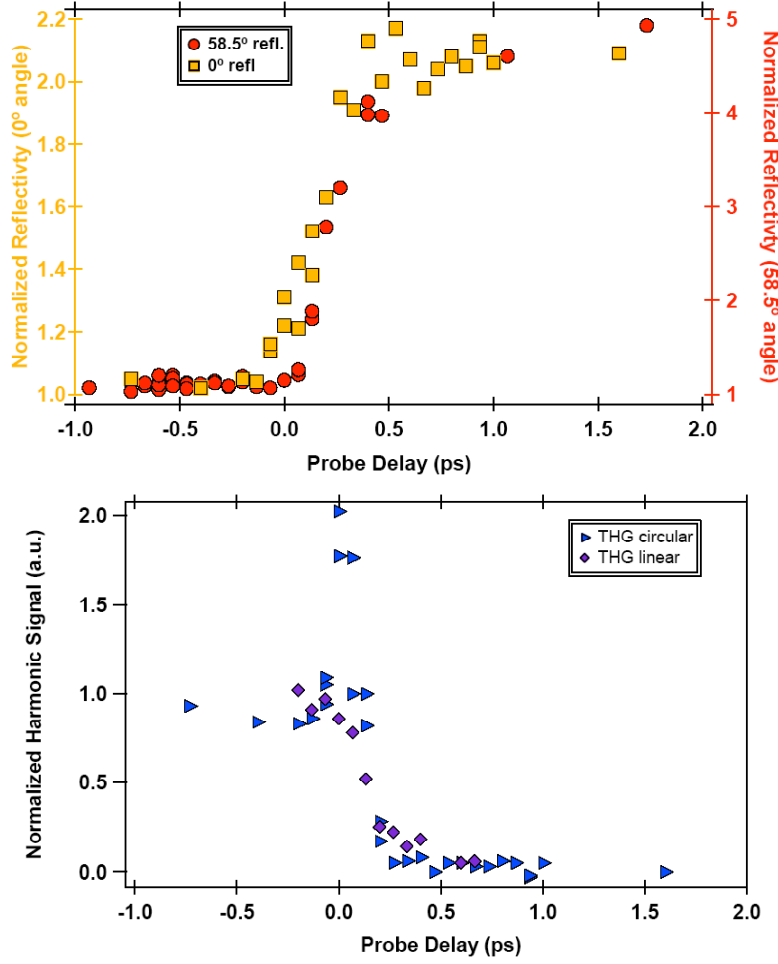
Figure 24: Reflectivity (top) and third harmonic signal (bottom) from two incident polarization configurations on the (100) surface of laser melted Si. The pump laser fluence was 310 mJ/cm².

The increase in reflectivity that we observe agrees within ~ 10% with calculations using the Fresnel equations to predict the change in reflectivity upon melting. This change is due to the dielectric constant approaching that of a liquid (Drude) metal. The linear dielectric constant affects harmonic generation at a surface through the linear Fresnel equations, which determine the penetration of the probe light into the material. The harmonic intensity is proportional to the fundamental field to the *2j* power, where *j* is the harmonic order, so the field amplitude has a large effect on the harmonic amplitude.

Our data are completely consistent with calculations for the expected ratios of reflectivity and THG. We must assume an oxide layer on the surface to model these data adequately. We observe similar drops in THG upon laser heating for linear and circularly polarized pulses. Our calculations indicate that the drop in THG is due not only to the loss of short range order as the crystal melts but also to a change in Fresnel factors. In other words, as the crystal becomes molten, the probe cannot penetrate as deeply into the now conducting crystal and the efficiency of THG drops. Nonetheless, these data indicate that the THG diagnostic is an unambiguous and clear signature of a laser induced phase change. We also note that the time scale over which we

23

observe a change in reflectivity is slower than the time scale for a drop in THG. For example in GaAs the reflectivity increase during melting occurs over a nearly 500 fs window. However the THG drops in around 200 fs. This again results from an interplay of the drop in nonlinear polarizability and reflection factors. Further analysis of this work is now ongoing to quantify this effect.

The main conclusion from these experiments is that the THG technique provides a very fast and unambiguous signature of melting in Si and GaAs.

V. Third Harmonic Probing of Shock Waves in Si

Motivated by these laser induced melting results we finally moved to study of shocks with THG. We chose to pursue this in Si crystals as we had developed good expertise in THG from Si. The down side is that Si is complicated by numerous pressure-induced phase transitions, potentially complicating interpretation of the data. These measurements were also complicated by the need for thin, smooth Si slabs. We had to spend some considerable time developing target fabrication techniques that would permit shock experiments in slabs only of a few tens of μm thick.

The solution to target fabrication that we settled on involved etching thick Si wafers to a desired thickness over a small window area. Our Si targets were made by etching a silicon-on-insulator wafer as illustrated in figure 25. The wafers used in these experiments were purchased from www.ultrasil.com, and consisted of a thick handle (~500 μm Si), a thin buried oxide (box, ~ 1-5 μm SiO$_2$), and a device of various thicknesses (10-95 μm Si). With an appropriately shaped mask, regions of the handle were etched away to reveal the box. With a different process, the exposed box was then etched away while leaving the Si unharmed to reveal a small section of the Si device layer. It is this device layer that served as the target. This technique allowed us to produce many individual target shot areas on one wafer. A photo showing a section of the wafer with many target sites is provided in figure 26.
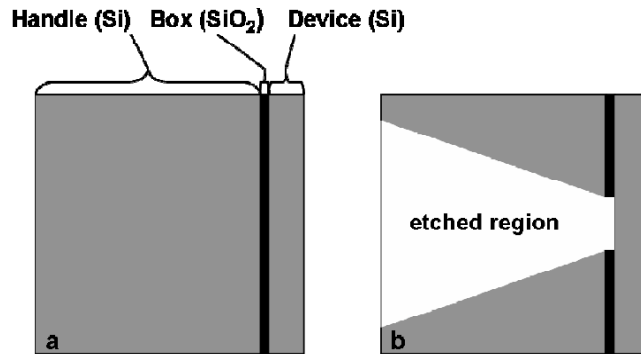

Figure 25: Illustration of how we produced sub-100 μm silicon targets for the Si shock experiments.

After completion of the etching processes, it was necessary to coat several skin depths of aluminum onto the front surface of the Si target so that the energy is absorbed at the surface, rather than throughout the bulk. This is because a shockwave is more quickly formed when energy is deposited in a smaller volume, rather than distributed over a larger volume, so it is better for the pump energy to encounter a material with short skin depth, rather than a long skin depth. We chose Al over Si since Al has a skin depth of 7.5 nm in 800 nm light while Si has an absorption depth of over ~ 10 μm. To ensure absorption at the surface by the rising edge of the pulse we typically used ~ 100 nm of aluminum as the absorptive layer.
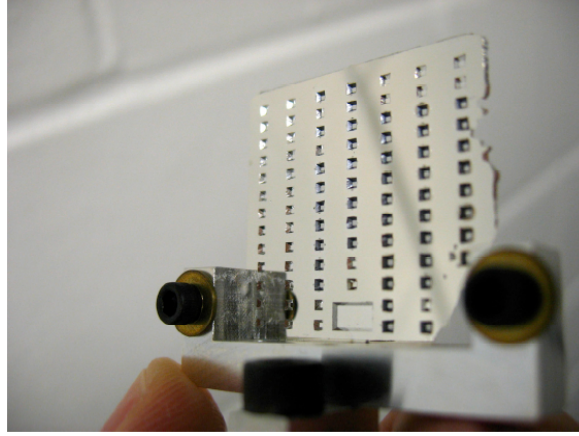

Figure 26: Photo of the etched Si target array.

An important complication in Si is that the lattice can compress elastically, along one dimension before is compresses hydrostacially (plastically). As the Hugoniot for Si illustrates (shown in figure 27) the elastic compression under shock loading will have a shock velocity that is nearly 9 km/s while the plastic compression will have a shock front slower than this, at least up to a peak shock pressure of about 750 kbar. We therefore expect an elastic precursor wave emerging before the main shock front.
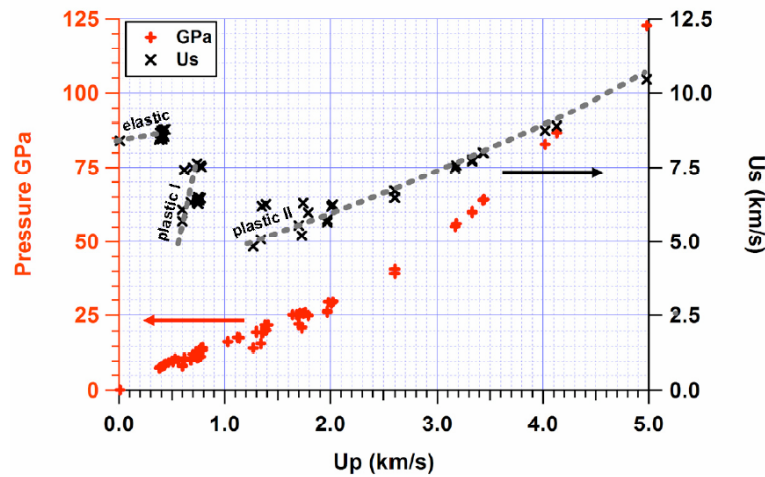

Figure 27: Hugoniot for Si (taken from ref [19]) showing the particle velocity (black) and shock pressure (red).

To explore the shock dynamics we undertook a series of 2D interferometry measurements from the back side of the Si wafer targets. Figure 28 shows characteristic expansion data from a 20 μm thick Si slab target. We see a small amount of expansion at early time followed by rapid expansion in the middle of the target approximately 1 ns later.
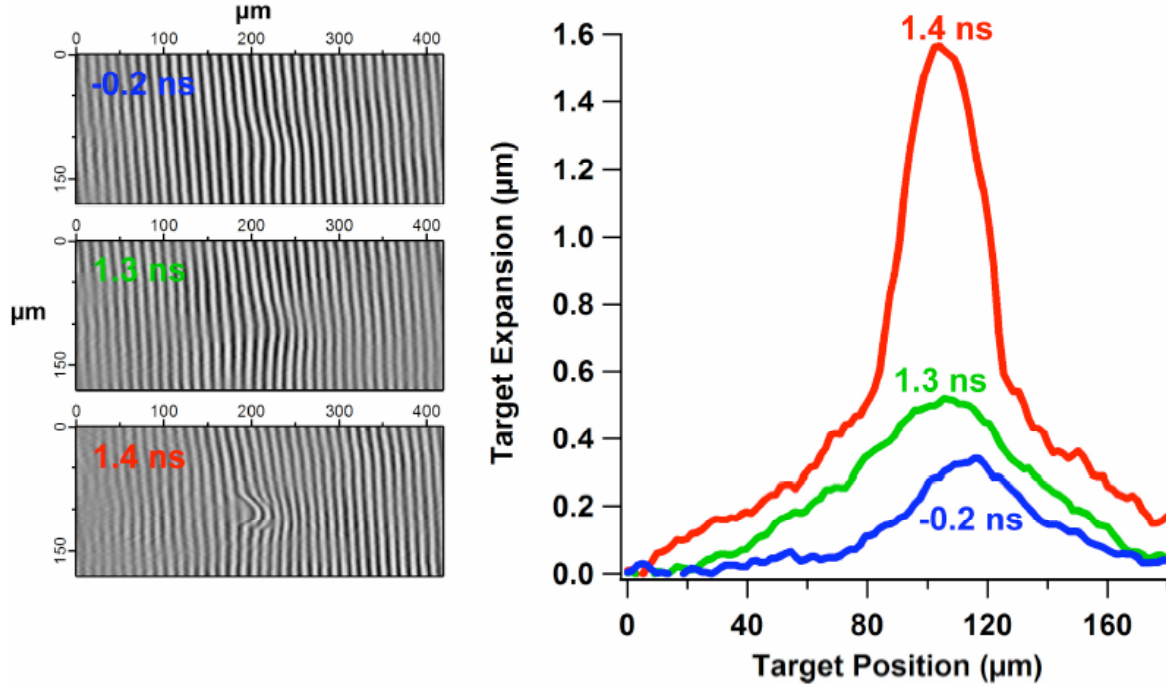

Figure 28: 2D interferometry data of a shock break out in 20 μm Si slabs driven by an intensity of 2 x 10^{13} W/cm^2. The right hand plots show the deconvolved expansion profiles at 3 times.

We conducted an extensive series of experiments measuring the expansion of shock release in Si targets of varying thickness and drive intensity. This allowed us to explore a range of shock parameters. Not only does changing the driven energy change the shock pressure but because the thicker Si slabs had a shock transit time longer than the drive pulse, the shock wave decayed resulting in a variation of shock pressure at the rear surface with different target thicknesses. The drive laser energy was ~ 750 mJ in varying spot sizes that resulted in laser intensities that varied between 1 x 10^{13} W/cm^2 and 2 x 10^{14} W/cm^2.

Measured expansion from the rear surface as a function of time for a variety of Si target thicknesses is illustrated in figure 29. In this figure, data located toward the right-hand side is generally from a thicker target, while data located toward the left-hand side comes a thinner target (as noted in the figure). The exceptions to this rule are the cases where the same target thickness was shot with different laser intensities. The higher intensities cause a higher pressure, which cause a higher shock velocity, which leads to an earlier shock breakout.

The yellow triangles represent data taken with 10 μm Si targets and a laser intensity of ~2 x 10^{14} W/cm^2. During these shots, the laser contained several ns-scale pre-pulses from a misalignment of a waveplate in the post-regen isolation stage. This led to pre-pulses with amplitudes of ~10^{-4}

times the main peak, located at 15, 30, and 45 ns before the peak. These pre-pulses caused significant preheating of the target and pre expansion by an additional 0.4 μm in the rear surface, as compared with data taken when the pre-pulses were minimized, shown in brown diamonds. Some pre expansion does still occur, as evidenced by about 0.5 μm of surface expansion the nanosecond before the main shock breaks out that the surface and expands at a velocity of ~ 4 km/s. This pre expansion, on the other hand, expands at around 0.2 km/s. We attribute this to the elastic wave, which precedes the shock at high shock velocity and low particle velocity (as illustrated by the Hugoniot curve in figure 27.) All of our data show this pre-expansion elastic precursor.

The dark blue squares in the graph represent data taken with 10 μm targets and a lower laser intensity of 2 x 10^{13} W/cm^2. The data with the pink triangles were taken with 20 μm targets and a laser intensity of 2 x 10^{14} W/cm^2. Despite the higher drive intensity of these data, the fact that the target is 20 μm instead of 10 μm thick leads to a break out velocity which is comparable to the 10 μm case.   The red circles represent data taken also with 20 μm thick targets but with a lower laser intensity of 2 x 10^{13} W/cm^2. These data show a clear two structure wave, the first with brake-out velocity of 0.14 km/s and the second main wave with velocity of 4 km/s. This shock suggests a particle velocity of 2 km/s and, therefore a shock pressure of 400 kbar [19].
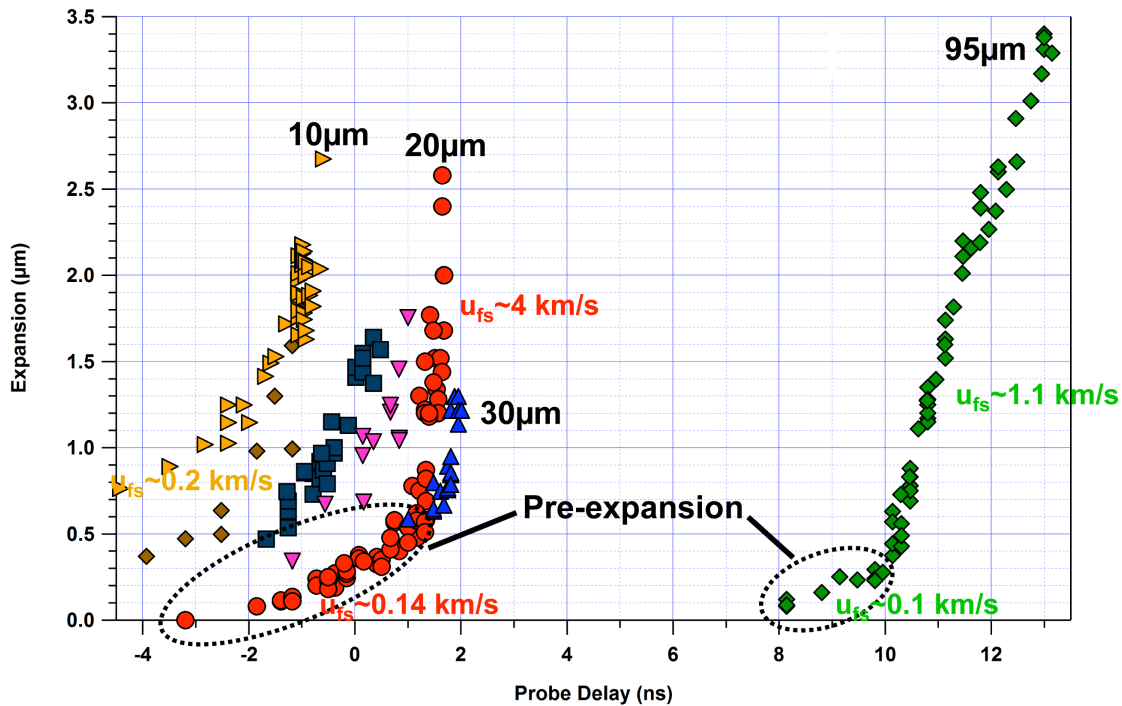

Figure 29: Plot of silicon peak expansion vs. probe delay under various conditions. Details of the various points are described in the text.

The blue triangles in figure 29 represent data taken with 30 μm targets and a laser intensity of 1 x 10^{14} W/cm^2. These data seem to cover the end of the pre-expansion and the very beginning of

the shock expansion. We can compare these data with the pink triangles to estimate the shock velocity at around 6-10 km/s, which bounds the published elastic sound speed of ~ 9 km/s for (100) silicon. In all of the above silicon experiments, the small spot-size combined with the slope of the target make it difficult to extract any expansion data from the interferograms above 1.5 to 2 μm expansion. Finally, the green diamonds represent data taken with 95 μm silicon and laser intensity of 6 x 10^{13} W/cm^2. The 1.1 km/s expansion velocity implies a shock pressure of only 100 kbar. This lower pressure results from the decay of the shock wave in time, as illustrated in figure 4.

We then turned to derive THG signal from these characterized Si shocks. These measurements were complicated by UV emission from the laser plasma at the front surface of the target. With careful baffling we succeeded in deriving clean THG signal from three different Si shock conditions. The first was the low pressure shock in the 95 μm Si targets. The expansion time history from this target is reproduced in figure 30 on top of the THG signal detected as a function of probe delay. Although there is some scatter in THG signal, it more or less remains constant throughout the expansion of the target over 3 μm. We can conclude, then, that we are observing in real time the Si expanding as a crystalline, well ordered structure, even though it has expanded significantly from its equilibrium surface position.
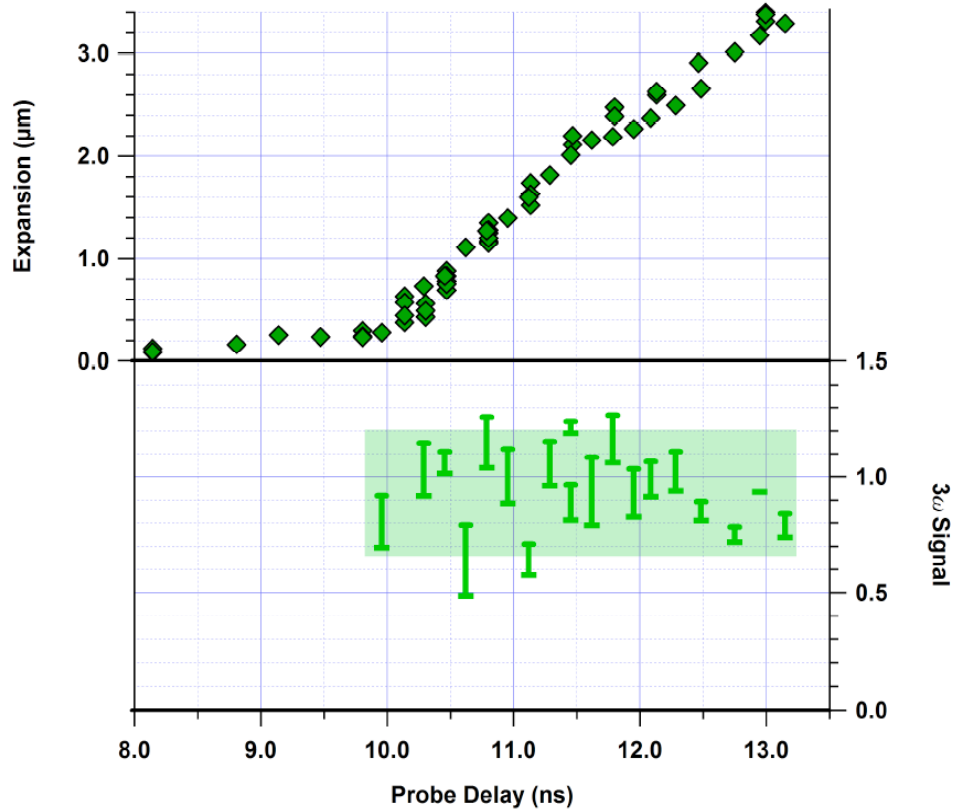

Figure 30: Measure time history of the expansion and THG from a 95 μm thick Si slab driven at 6 x 10^{13} W/cm^2. The plot on the top reproduces the back surface expansion history and the bottom plot shows the THG signal over the same time window.

This time history is quite different in targets in which the shock pressure is higher. Figure 31 illustrates the same juxtaposition of expansion and THG signal for two other situations: a 20 μm target irradiated at 2 x 10^{13} W/cm^2 (red circles) and the 30 μm thick target irradiated at 1 x 10^{14}. The observed particle velocity (2 km/s) indicates that both of these shocks have a peak pressure in the vicinity of 400 kbar. In both cases, the THG signal remains strong during the slow preexpansion of the target, indicating that the Si remains crystalline during this phase. However, the THG then rapidly falls once the main shock emerges. The time at which this fall starts is about 500 ps later in the 30μm target than in the 20 μm target because of the longer time for the shock to transit the slab.

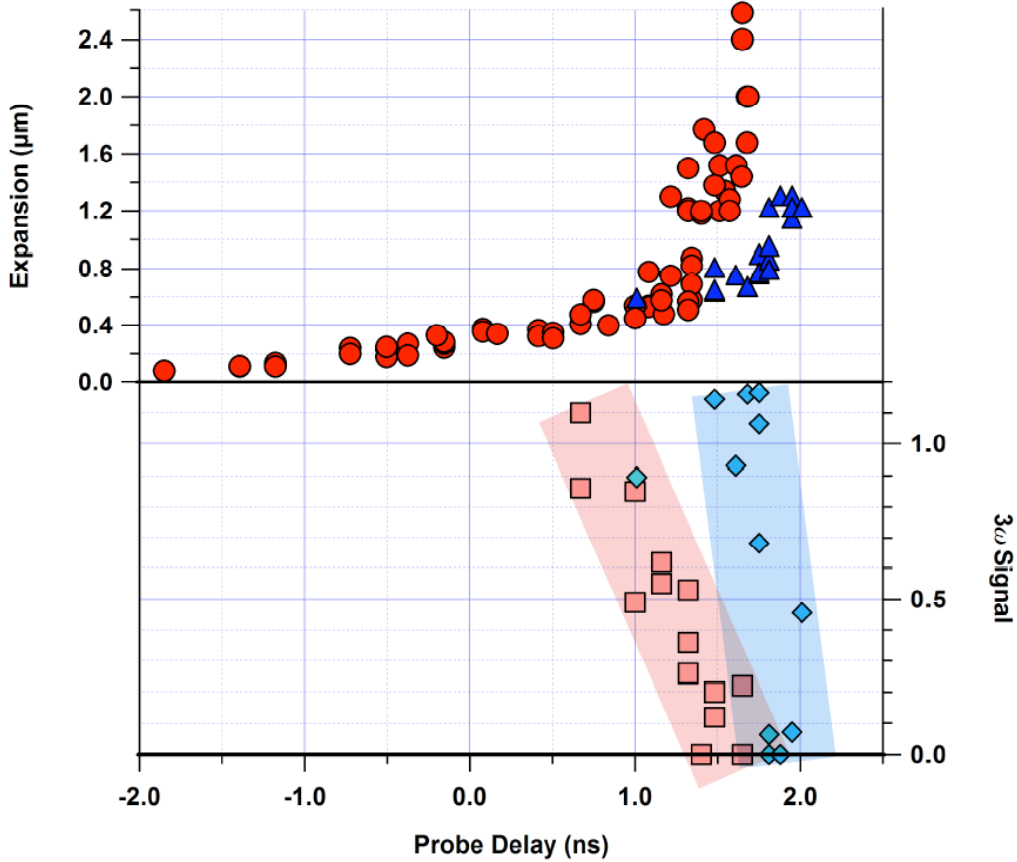*Figure 31: Measured time history of the expansion and THG from 20 and 30 μm thick Si slabs driven at 2 x 10^{13} W/cm^2 in the first case and 1 x 10^{14} W/cm^2 in the second. The plot on the top reproduces the back surface expansion histories and the bottom plot shows the THG signal over the same time window.*

This result is remarkable as it tells us that in real time, over a time span of less than 500 ps, the Si must become disordered in some way. This is surprising at first because a 400 kbar shock is not sufficient to melt the Si. However, we surmise that there may be some solid-to-solid phase change which serves to randomize the lattice under shock compression to 400 kbar, affecting the

THG dramatically. We have carefully considered the possibilities that our THG collection is affected by scatter or collection f/#. We have at this point concluded that the fall in THG signal must be attributed to microstructure changes in the shocked Si. This represents, to our knowledge, the first real time in situ observation of picosecond time scale phase change dynamics in laser shocked crystals diagnosed by optical means.

VI. Summary

We can summarize the work undertaken within this past grant period by three significant findings and advances:

1) We can produce and control the pressure of table top laser-driven shocks in μm-scale targets with pressure up to 1 Mbar. These shocks match well to the predictions of Lagrangian hydrodynamics codes.
2) Third harmonic generation can yield an unambiguous signature of dynamic melting in a crystal as evidenced by laser induced melting experiments in Si and GaAs.
3) Third harmonic generation has been used to observe expanding Si and shown that at pressures near the elastic to plastic transition the Si remains crystalline while at shock pressures above that limit but still well below melting the crystal undergoes significant disordering.

References

1. Mabire, C. and P.L. Hereil, *Shock induced polymorphic transition and melting of tin up to 53 GPa (experimental study and modelling)*. Journal De Physique Iv, 2000. **10**(P9): p. 749-754.
2. Barker, L.M., *Shock-Wave Study Of Alpha - Epsilon Phase-Transition In Iron*. Bulletin Of The American Physical Society, 1975. **20**(1): p. 25-25.
3. Swift, D.C., et al., *Dynamic response of materials on subnanosecond time scales, and beryllium properties for inertial confinement fusion*. 2005. **12**(5).
4. Asay, J.R., *Experimental Determination Of Shock-Induced Melting In Aluminum*. Bulletin Of The American Physical Society, 1975. **20**(1): p. 20-20.
5. Werdiger, M., et al., *Detecting of melting by changes of rear surface reflectivity in shocked compressed metals using an interferometric diagnostic method*. Laser and Particle Beams, 1999. **17**(3): p. 547-556.
6. Elias, P., P. Chapron, and B. Laurent, *Detection of Melting in Release for a Shock-Loaded Tin Sample Using the Reflectivity Measurement Method*. Optics Communications, 1988. **66**(2-3): p. 100-106.
7. Yakovlev, V.V. and S.V. Govorkov, *Diagnostics of surface layer disordering using optical third harmonic generation of a circular polarized light*. Applied Physics Letters, 2001. **79**(25): p. 4136-4138.
8. M. Born and E. Wolf, *Principles of Optics: Electromagnetic Theory of Propagation Interference and Diffraction of Light*, (Oxford: Pergamon Press, 1980), p51
9. R. W. Boyd, *Nonlinear Optics*, (Boston: Academic Press, 1992).

10. J. T. Larsen and S. M. Lane, J. Quant. Spectrosc. Ra **51**, 179 (1994).
11. Y. B. Zel'dovich and Y. P. Raizer, "Physics of Shock Waves and High-Temperature Hydrodynamic Phenomena", edited by W. D. Hayes and R. F. Probstein, Dover Publications, New York (2002).
12. Jankowski, A., J. Ferreira, et al. (2005). "Activation energies of grain growth mechanisms in aluminum coatings." Thin Solid Films **491**(1-2): 61-65.
13. Takeda, M., H. Ina, et al. (1982). "Fourier-Transform Method Of Fringe-Pattern Analysis For Computer-Based Topography And Interferometry." Journal Of The Optical Society Of America **72**(1): 156-160.
14. Bushman, A. V., I. V. Lomonosov, et al. (2003). "Shock Wave Database." from http://teos.ficp.ac.ru/rusbank/index.php?text=1.
15. Lyon, S. P. and J. D. Johnson (1992). "Sesame: Los Alamos National Laboratory Equation of State Database." Los Alamos report **LA-UR-92-3407**.
16. Saeta, P., J. K. Wang, et al. (1991). "Ultrafast Electronic Disordering During Femtosecond Laser Melting Of Gaas." Physical Review Letters **67**(8): 1023-1026.
17. Tom, H. W. K., G. D. Aumiller, et al. (1988). "Time-resolved study of laser-induced disorder of Si surfaces." Physical Review Letters **60**(14): 1438.
18. Sokolowski-Tinten, K. and D. von der Linde (2000). "Generation of dense electron-hole plasmas in silicon." Physical Review B **61**(4): 2643-2650.
19. Goto, T., T. Sato, et al. (1982). "Reduction of Shear-Strength and Phase-Transition in Shock-Loaded Silicon." Japanese Journal of Applied Physics Part 2-Letters **21**(6): L369-L371.